Influence of laminated architectures of heterostructured CeO2-ZnO and Fe2O3-ZnO films on photodegradation performances

Zexin Yu, Bilel Chouchene, Meimei Liu, Hatem Moussa, Raphaël Schneider, Michel Moliere, Hanlin Liao, Yao Chen, Lining Sun

Influence of laminated architectures of heterostructured CeO_2-ZnO and Fe_2O_3-ZnO films on photodegradation performances

Zexin Yu[ac]*, Bilel Chouchene[b], Meimei Liu[a]*, Hatem Moussa[b], Raphaël Schneider[b]*, Michel Moliere[a], Hanlin Liao[a], Yao Chen[c], Lining Sun[c]

[a] *ICB UMR 6303, CNRS, site de UTBM, Université de Bourgogne Franche-Comté, 90010 Belfort, France*

[b] *Université de Lorraine, CNRS, LRGP, 54001 Nancy, France*

[c] *School of Mechanical and Electrical Engineering, Soochow University, 215123 Suzhou, China*

* *Corresponding authors.*

E-mail addresses: zxyu@suda.edu.cn (Zexin Yu), meimei.liu@utbm.fr (Meimei Liu) raphael.schneider@univ-lorraine.fr (Raphaël Schneider).

Abstract

The development of photocatalytically active films has gained a great attention in recent years. Herein, new heterostructured films associating ZnO and CeO_2 or Fe_2O_3 and exhibiting ~~CeO_2-ZnO and Fe_2O_3-ZnO films with~~ various architectures were prepared by the solution precursor thermal spray (SPPS) process. ~~To the best of our knowledge, this report is the first to examine~~ The paper examines the effect of the films laminated architectures on the photodegradation performance. For CeO_2-ZnO and Fe_2O_3-ZnO films, the photodegradation efficiency of the Orange II dye is 100% and 95% after 240 min UV light irradiation and after 360 min visible light irradiation, respectively. ~~the UV-light-driven photodegradation efficiency towards the Orange II dye was up to 100% within 240 min and the visible-light-driven photodegradation efficiency was as high as~~

~~95% within 360 min~~. ~~The laminated architectures are dependent on the materials used to construct the heterostructured catalysts~~. The photocatalytic activity of the laminated structures was found to depend on the materials used to construct the heterostructured catalysts. For CeO_2 which exhibits a good photoactivity, intermediately-laminated architecture was demonstrated to play a key role. By contrast, a non-laminated architecture is more suitable for materials exhibiting a modest photocatalytic activity (Fe_2O_3, $ZnFe_2O_4$). This study describes a novel route for depositing photocatalytically active laminated films and the influences of their structures on the photocatalytic performance. ~~not only describes a novel route for the development of photocatalytically active laminated films, but provides also insights into the effects of the architectures on the photocatalytic performances of the films~~.

Keywords: Solution precursor plasma spray; laminated architectures; heterostructured films; nanostructures; photodegradation

1. Introduction

Due to the industrial development, population growth and increasing consumptions of chemicals, water pollution has become a pervasive threat in our daily life [1]. Therefore, many studies were devoted to the treatment of contaminated water. Among methods developed, advanced oxidation processes (AOPs) are efficient options to decontaminate water, especially to degrade organic pollutants residues [2]. The photocatalytic degradation (PCD) is an AOP receiving great attention because it does not require extra chemical reagents and uses only light to promote the decomposition of pollutants into water and carbon dioxide [3].

ZnO is one of the most promising metal oxide photocatalysts, thanks to its high activity, availability, low cost and stability [4]. In order to improve its photodegradation efficiency, pure ZnO photocatalysts were developed with various surface morphologies, including 0-D spherical nanoparticles [5], 1-D nanorods [6], nanowires [7], nanosheets [8], 2-D nanobelts [9] and 3-D hierarchical complex architectures [10]. For example, improved charge carriers separation was observed in 1-D ZnO nanostructures due to their high aspect ratios and to the exposition of specific crystal planes [11-13].

Although the optimization of ZnO particles morphology is able to make substantial improvements on the photocatalytic activity, ZnO suffers from ~~the limited absorption of photon energy due to~~ its wide bandgap of 3.37 eV (367 nm) which limits its light absorption to the UV region [14]. To overcome this drawback, the association of ZnO with ~~lower~~ narrower bandgap semiconductors, e.g. CuO or Fe_2O_3, has been reported for PCD applications [15-17]. Recently, CeO_2 has also attracted a lot of attention for photocatalytic applications due to its ~~unique f and d electron orbital structure, UV absorbing ability,~~ high thermal stability, high electrical conductivity and its ability to promote electron transfer reactions ~~large oxygen storage capacity~~ [18, 19]. Fe_2O_3 is also of high interest because it is cheap, earth-abundant and of ~~low~~ narrow bandgap (ca. 2.2 eV) and thus allows to improve the visible light-driven photocatalytic activity [15, 20]. Thus, heterostructured

CeO_2-ZnO and Fe_2O_3-ZnO photocatalysts were demonstrated ~~found~~ to exhibit high activity in PCD [19, 21-23] due to the improved UV and visible-light harvesting ability but also because the electron-hole pairs separation is improved.

It should be noted that the use of nanopowders for PCD requires a post-filtration before the reuse and the loss of catalyst may rise potential environmental and health risks [24, 25]. For this reason, film-formed photocatalysts are of higher potential in practical photocatalytic applications [26-28]. Laminated architectures in these films affect their performances, including the antifungal activity [29], the optical absorption [30], and the dielectric properties [31]. The influence of the structure of the laminated layers on their photocatalytic performances has been observed for spherical polyaniline@titania powders [32]. However, only a few reports about laminated films for photocatalytic applications have been published [33, 34], and the influence of their structuration on the photocatalytic performances was only briefly investigated.

In this work, we report the influence of laminated architectures within heterostructured CeO_2-ZnO and Fe_2O_3-ZnO films on their photocatalytic activities. The films were prepared by a ~~facile~~ deposition method, named "Solution Precursor Plasma Spray" (SPPS), which is fully described in our previous study ~~studies~~ [28]. The various ~~laminated~~ films' architectures were prepared ~~realized~~ by alternately injecting zinc and cerium/iron precursors solutions with designed cycles. All heterostructured CeO_2-ZnO and Fe_2O_3-ZnO films were characterized by scanning electron microscopy (SEM), X-ray diffraction (XRD) and Raman spectroscopy. UV-visible absorption spectroscopy was also used to estimate their energy bandgap ~~bandgaps~~. The photocatalytic performances of those laminated films were evaluated through the degradation of the Orange II dye solution under UV or visible light radiation ~~illumination~~. The role played by the various active species involved in PCD was also investigated.

2. Experimental

2.1. Solution precursor preparation

For forming ZnO, CeO_2, and Fe_2O_3 composites, ~~the~~ zinc nitrate hexahydrate ($Zn(NO_3)_2{\cdot}6H_2O$, Sigma-Aldrich, purum, ≥ 98%), cerium (III) nitrate hexahydrate ($Ce(NO_3)_3{\cdot}6H_2O$, Alfa Aesar, 99.5%) and iron nitrate nonahydrate ($Fe(NO_3)_3{\cdot}9H_2O$, Sigma-Aldrich, 98.0%-101.0%) were used as solutes respectively to prepare the precursor solutions. For all the laminated composited films, the ratios of Ce/Zn and Fe/Zn in mole the raw precursors solutions were always set as 20%. The concentrations for Zn(OAc), $Ce(NO_3)_3$ and $Fe(NO_3)_3$ solution dissolved in a 1:3 water: ethanol mixture ~~mixture of water and ethanol~~ are 0.2 M, 0.04 M and 0.04 M, respectively.

2.2. Plasma spray conditions

The deposition of the ~~those~~ laminated composite films was ~~will be~~ conducted by a F4 direct current (DC) plasma torch (Oerlikon Metco, Switzerland) under atmospheric conditions via the SPPS technique. For the photodegradation tests, the stable alumina plates (33 mm x 34 mm x 2 mm) were used as substrates. To control moving trajectory and velocity of the deposition procedures, the F4 torch was fixed to a robotic arm (ABB, Switzerland). The injection ~~Injection~~ of as-prepared solutions was ~~were~~ driven by pressured N_2 ~~nitrogen~~ gas~~, where~~ and a stainless steel injector was used. ~~For better maintaining the same deposition conditions, a homemade device was employed to measure and control the distance and angle between the solution injector and the nozzle of F4 torch.~~ For the other plasma spraying parameters, including gas flow rates of Ar and H_2, spraying distance, electric current and deposition cycles, the same conditions were used as listed in Table 1 ~~values were selected~~. The heterostructured CeO_2-ZnO and Fe_2O_3-ZnO films with various laminated architectures were prepared by different injection modes, including mixtures of precursor solutions and separated injections strategies. Fig. 1 shows the schematic distribution patterns of CeO_2-ZnO and Fe_2O_3-ZnO films with various architectures. In the CeO_2-ZnO-M and Fe_2O_3-ZnO-M notation, “M” stands for the mixed solution of precursors. For the laminated CeO_2-

ZnO-S3, CeO_2-ZnO-S6 and CeO_2-ZnO-S12 films (as well as Fe_2O_3-ZnO-S3, Fe_2O_3-ZnO-S6 and Fe_2O_3-ZnO-S12 films), the notation "S" stands for "separated solution", and the numbers 3, 6 and 12 refer to the number of layers per cycle. The deposition strategies for different laminated CeO_2-ZnO and Fe_2O_3-ZnO films were schematically illustrated in Fig. 2. The detailed spraying parameters are summarized in Table 1.

2.3. Characterization of the coatings

Scanning electron microscopy (SEM, JEOL, JSM-5800LV) was used to observe the surface morphologies of the ~~these~~ heterostructured CeO_2-ZnO and Fe_2O_3-ZnO films. ~~A~~ X-ray diffraction (XRD, Bruker AXS D8 focus, Germany) using a cobalt anticathode (λ = 1.78897 Å) was used ~~employed~~ to determine ~~detect~~ the phase compositions of these samples under a scanning rate of 0.1 °/s. An XploRA PLUS Raman Microscope (Horiba Jobin Yvon) was used to analyze the structure of as-deposited films based on their Raman spectra (a laser emitting at 532 nm was used). ~~An XploRA PLUS Raman Microscope (Horiba Jobin Yvon) was further used to analyze the composition of as-deposited films based on their Raman spectra with an excitation at 532 nm.~~ UV-visible absorption and diffuse reflectance spectra of heterostructured CeO_2-ZnO and Fe_2O_3-ZnO films with different laminated architectures were recorded ~~recoded~~ via a UV-vis spectrophotometer (Shimadzu, UV-2600). The bandgap energy values of the films were estimated using the Kubelka-Munk function F(R) according to equation (1) ~~Then the values of bandgaps of those films were estimated based on Kubelka-Munk equation by the Tauc plots~~ [35].

$$F(R) = \frac{(1-R)^2}{2R} \qquad (1)$$

where R is the reflectance. E_g values of heterostructured CeO_2-ZnO and Fe_2O_3-ZnO films were determined by plotting $[F(R)hv]^2$ vs hv (*h* is the Planck's constant and *v* is the light frequency) and extrapolating the tangents to the x axis.

2.4. Photocatalytic ~~performances~~ characteristics

The photocatalytic activities of these laminated samples were measured by the photodegradation of the Orange II dye (5 mg/L) under UV and visible light illumination ~~illuminations~~ (Hg-Xe lamp with 15 mW/cm^2 and Xe lamp with 7.5 mW/cm^2, respectively) at room temperature. The ~~degraded~~ solutions were analyzed ~~by~~ using a UV–vis spectrophotometer (Thermo Scientific Evolution 220). In a typical test, five identical film samples with 60 mg of photocatalyst were placed into a Petri dish containing 60 mL of the Orange II aqueous solution. To avoid the influence of adsorption ~~absorption~~ on the evaluation of photodegradation percentage, the samples were immersed in the Orange II solution for 120 min in the dark with magnetically stirring to reach ~~for~~ the adsorption-desorption equilibrium. ~~At each one~~ Each hour, 1 mL of the liquid was extracted to evaluate the remaining concentration of Orange II by measuring its absorption peak at 485 nm. The photodegradation performances and the pseudo-first-order kinetics were calculated based on the equations (2) ~~(1)~~ and (3) ~~(2)~~, respectively [36, 37]:

$$D(\%) = \frac{C_0 - C_t}{C_0} \times 100 \qquad (2)\ \textit{~~Eq(1)~~}$$

$$\ln\left(\frac{C_0}{C_t}\right) = k_{app}t \qquad (3)\ \textit{~~Eq(2)~~}$$

where C_0 is the initial concentration of Orange II, C_t is the concentration of Orange II after the irradiation time t, and k_{app} is the reaction rate constant (min^{-1}), respectively.

2.5. Determination of reactive species

To identify the active species involved in ~~for~~ the photocatalytic reaction, various scavengers, including *tert*-butanol (*t*-BuOH, 10 mM), *p*-benzoquinone (BQ, 0.1 mM), ammonium oxalate monohydrate (AO, 10 mM) and dimethyl sulfoxide (DMSO, 10 mM) were separately introduced into the Orange II solution before illumination. These scavengers will trap the active species

(electrons, holes, hydroxyl and superoxide radicals) involved in the photodegradation of the dye. The trapping tests were conducted under UV light irradiation as described previously.

3. Results and discussion

3.1 Phase composition of CeO_2-ZnO and Fe_2O_3-ZnO films with different laminated architectures

The XRD patterns of the CeO_2-ZnO and Fe_2O_3-ZnO films with different architectures are shown in Fig. 3a and Fig. 3c. For CeO_2-ZnO samples, the characteristic XRD peaks of ZnO (PDF 75-0576), CeO_2 (PDF 78-0694) as well as of the Al_2O_3 substrate (PDF 81-2267) were detected (Fig. 3a). Due to the lower concentration of the cerium solution (0.04 M) compared to the zinc solution (0.2 M), a weak intensity was observed for CeO_2 peaks in the ~~these~~ XRD patterns. In addition, the XRD peaks of the CeO_2 phase in the CeO_2-ZnO-M sample are wider than that in the other laminated CeO_2-ZnO films, indicating smaller crystal sizes based on the Scherrer formula. This was confirmed by SEM results (*vide infra*). To confirm the presence of the ZnO and CeO_2 phases in the laminated CeO_2-ZnO films, Raman analyses were also performed (Fig. 3b). The peak at 467 cm^{-1} corresponds to the CeO_2 phase [38] while the signal located at 438 cm^{-1} is typical of the ZnO phase [39].

The laminated Fe_2O_3-ZnO films with different architectures were also characterized by XRD for their phase compositions. As shown in Fig. 3c, the XRD patterns of ZnO (PDF 75-0576), Fe_2O_3 (PDF 25-1402), $ZnFe_2O_4$ (PDF 77-0011) and of the Al_2O_3 substrate (PDF 81-2267) were observed in the heterostructured Fe_2O_3-ZnO samples. Due to the weak intensities of Fe_2O_3 and $ZnFe_2O_4$ phases, Raman analyses were also conducted to investigate the structures of Fe_2O_3-ZnO films (Fig. 3d). The peaks located at 330, 380, 437 and 578 cm^{-1} correspond to the ZnO phase [40]. The Raman modes of Fe_2O_3 phase are centered at 125, 141, 162, 508, 664 and 835 cm^{-1} [41]. The signals at 221, 246, 290, 350, 451, 487 and 647 cm^{-1} belong to the $ZnFe_2O_4$ phase [42], obtained by the *in situ* reaction between ZnO and Fe_2O_3 during the deposition as discussed in our

previous study [43]. In accordance with the XRD patterns, the underlying Al_2O_3 substrate was also detected in the Raman spectra (signals located at 416 and 750 cm^{-1}) [44]. XRD and Raman results confirm that CeO_2-ZnO and Fe_2O_3-ZnO films with various architectures ~~depending on the injection modes~~ were successfully prepared.

3.2 Influence of the injection modes on the surface morphologies of CeO_2-ZnO and Fe_2O_3-ZnO films

The effects of the injection modes on the surface morphologies of the CeO_2-ZnO and Fe_2O_3-ZnO films were investigated by SEM (see Fig. 4 and 5). With respect to the solution precursor as feedstock and the heating procedure, the SPPS process is similar to the spray pyrolysis technologies. It has been reported that the nucleation from the solution precursors is the first stage of the formation of metal oxides [45]. First, for the non-laminated CeO_2-ZnO-M sample prepared from the mixed precursors solution, the usually observed cauliflower-like morphologies composed of irregular particles were observed (Fig. 4a-b). Previous studies demonstrated that the presence of some metal salts (Li^+, Na^+ or Cu^{2+}) in the precursor solution may influence the shape of the particles formed [14, 46].

By contrast, for intermediately-laminated like CeO_2-ZnO-S3 or CeO_2-ZnO-S6 films, rod-like microstructures, marked by red circles, were observed (Fig. 4c-f). In accordance with our previous study [43], the formation of these rods-like microstructures is attributed to the separated injection mode of the precursors. Therefore, it is likely that the rod-like microstructures in the CeO_2-ZnO films could be attributed to the ZnO phase. Besides, for the full-laminated sample (i.e. CeO_2-ZnO-S12), no rods-like structures were detected (Fig. 4g-h). However, based on our report [47], the rod ~~rods~~-like microstructures can be masked ~~hidden~~ by the covering CeO_2 layer. This is indirectly proven by the XRD patterns of the CeO_2-ZnO films (Fig. 3a), in which ~~stronger intensities of the~~ CeO_2 peaks with a higher intensity compared to those of the mixed metal oxides

(e.g. CuO, Fe_2O_3, Co_3O_4) can be observed [47]. In addition, when comparing the CeO_2-ZnO-S6 with the CeO_2-ZnO-S3 film, the length of each rod is smaller in the latter one, suggesting that the increase of the deposition cycles within each injection turn promotes the growth of rods. Finally, fine particles could also be observed in the laminated CeO_2-ZnO-S3/S6/S12 samples (Fig. 4d, 4f, 4h), which may correspond to the CeO_2 phase. Moreover, for the CeO_2-ZnO-S3 and CeO_2-ZnO-S6 samples, the small CeO_2 particles were distributed on the surface of ZnO rod-like structures, suggesting a good contact between ZnO and CeO_2 phases.

The SEM-associated EDS analyses were used to evaluate the Zn/Ce ratios in the heterostructured CeO_2-ZnO films with different laminated architectures (Fig. S1). From the non-laminated pattern (i.e. CeO_2-ZnO-M sample) to the full-laminated pattern (i.e. CeO_2-ZnO-S12 sample), the Zn/Ce ratio decreased from ca. 7.0 to 2.82, suggesting that less ZnO is present at the surface of these films, which is in good agreement with the spraying patterns used.

The surfaces of the non-laminated Fe_2O_3-ZnO-M sample and of the intermediately-laminated Fe_2O_3-ZnO-S3 sample are composed of irregular particles (Fig. 5a-d). Fe_2O_3-ZnO-S6 and Fe_2O_3-ZnO-S12 samples contain more rods (Fig. e-h, as marked by red rectangles). A similar trend was observed for CeO_2-ZnO samples for which rod-like microstructures were observed in the intermediately-laminated and fully-laminated architectures (i.e. Fe_2O_3-ZnO-S6 and Fe_2O_3-ZnO-S12 samples).

Finally, a representative cross-section SEM picture of the Fe_2O_3-ZnO-S12 sample is shown in Fig. S2. As can be seen, after 12 cycles of deposition, the thicknesses of the ZnO layer and of the Fe_2O_3 layer are of ca. 1.4 μm and 1.1 μm, respectively. Since all the spraying parameters were constant during the deposition, its efficiency should be theoretically the same for each deposition cycle. Thus, the thickness of a ZnO layer per deposition cycle is around 0.12 μm and the thickness of a Fe_2O_3 or CeO_2 layer per deposition cycle is about 0.9 μm.

3.3 Optical performance of laminated CeO_2-ZnO and Fe_2O_3-ZnO films

In order to investigate the light absorptivity of the CeO_2-ZnO and Fe_2O_3-ZnO films, their UV-visible absorption spectra were recorded (Fig. S2a and Fig. S2c, respectively). As previously mentioned ~~afore-mentioned~~, pure ZnO absorbs only in the UV region ($\lambda < 368$ nm) due to its wide bandgap (3.37 eV). Thanks to the formation of an heterostructured material associating CeO_2 and ZnO, the absorption in the visible domain slightly increases (Fig. 6a). A significantly higher absorption in the visible light range was observed for the laminated Fe_2O_3-ZnO samples (Fig. S3c ~~S2c~~), due to the low bandgap of Fe_2O_3 (~2.2 eV). The corresponding UV-visible diffuse reflectance spectra of CeO_2-ZnO and Fe_2O_3-ZnO films are displayed in Fig. S3b ~~S2b~~ and Fig. S3d ~~S2d~~. Using the Kubelka–Munk function [26], the bandgap values (*Eg*) were determined by extrapolating ~~extrapolation of~~ the plots of $(F(R)\times h\nu)^2$ *vs* hν towards the x-axis (Fig. 6a-b). For CeO_2-ZnO films, the bandgap increased from 3.10 eV for CeO_2-ZnO-M to 3.31 eV for CeO_2-ZnO-S12. The CeO_2-ZnO-M film ~~films from the mixture solution~~ exhibits the narrowest bandgap (3.10 eV), ~~due to the heterostructured film formed between CeO_2 and ZnO,~~ which suggests that the use of the mixed-solution is more suitable than the separated-injection mode for minimizing the bandgap of the films. ~~The~~ An increasing bandgap energy ~~of bandgaps~~ was also observed in the Fe_2O_3-ZnO films from the non-laminated architecture ~~(mixture solution)~~ and to the fully-laminated architecture ~~(totally separated injection mode)~~. The bandgaps of Fe_2O_3-ZnO films ranged from 2.65 eV to 2.93 eV (Fig. 6b). From the point of view of photon energy absorption, the composite films prepared from the mixture solution should exhibit a higher photoactivity under visible light irradiation. However, when considering the surface morphologies, the composite films prepared via the separated-injection mode expose highly-active crystal planes, which should also enhance the photocatalytic activity. The influence of these parameters will be compared and discussed (*vide infra*).

3.4 Influence of films architecture on the photodegradation efficiency under UV light

The photocatalytic activities of CeO_2-ZnO and Fe_2O_3-ZnO films were first compared in the degradation of the Orange II dye under UV light irradiation. The evolutions of the UV-visible absorption spectra of Orange II are shown in Fig. ~~S3~~ S4a–d and Fig. ~~S3~~ S4e-h, respectively. The characteristic absorption peak of Orange II located at 485 nm gradually decreases with the irradiation time, indicating the degradation of Orange II in the presence of all CeO_2-ZnO and Fe_2O_3-ZnO films.

The plots of C_t/C_0 vs irradiation time for CeO_2-ZnO samples with the different architectures are displayed in Fig. 7a. For better comparison of their photodegradation efficiencies, the magnified area ranging from 180 to 240 min was inserted in Fig. 7a. Results show that Orange II was almost quantitatively decomposed ~~degraded~~ by the CeO_2-ZnO-S3 and CeO_2-ZnO-S6 samples after 240 min of UV light irradiation. The performances of CeO_2-ZnO-M and CeO_2-ZnO-S12 are slightly lower after the same irradiation time (96 and 93%, respectively). The better performances of CeO_2-ZnO-S3 and CeO_2-ZnO-S6 samples likely originate from the presence of rods-like microstructures and from the optimal association between CeO_2 and ZnO. The lower photodegradation efficiency observed for the CeO_2-ZnO-S12 sample may be due to the thick CeO_2 layer covering the ZnO phase. The pseudo-first-order kinetics of the photodegradations confirm these results and the following classification can be made: CeO_2-ZnO-S6 (0.0268 min^{-1}) > CeO_2-ZnO-S3 (0.0216 min^{-1}) > CeO_2-ZnO-M (0.0153 min^{-1}) > CeO_2-ZnO-S12 (0.0115 min^{-1}) (Fig. 7b), which consistent with the photodegradation results described in Fig. 7a.

The plots of C_t/C_0 versus irradiation time for Fe_2O_3-ZnO samples are shown in Fig. 7c. Compared to CeO_2-ZnO films, the photodegradation efficiencies under UV light irradiation were significantly more sensitive to the architectures of these films. For example, the Fe_2O_3-ZnO-M film is able to degrade almost 100% Orange II within 240 min, while only 21% degradation was achieved by the Fe_2O_3-ZnO-S6 sample.

These results are in good accordance with the intrinsic photocatalytic activities of ZnO, CeO_2 and Fe_2O_3. ZnO and CeO_2 exhibit both good quantum efficiency and valence bands with strong oxidation abilities. By contrast, Fe_2O_3 and $ZnFe_2O_4$ suffer from their poor photoelectric conversion and low valence band potential [48-50], indicating limited utilization of photogenerated-holes and electrons and low oxidizing ability. This may explain why Fe_2O_3-ZnO samples exhibit a lower activity than CeO_2-ZnO films. As shown in Fig. 7c, the photodegradation efficiencies follow the order: Fe_2O_3-ZnO-M (100%) > Fe_2O_3-ZnO-S12 (83%) > Fe_2O_3-ZnO-S3 (65%) > Fe_2O_3-ZnO-S6 (21%). The high performance of the Fe_2O_3-ZnO-M sample is attributed to the optimal association of ZnO and Fe_2O_3 (or $ZnFe_2O_4$) phases to form an heterostructured catalyst, suggesting the efficient offsetting of the weak use of photogenerated electron/hole pairs from Fe_2O_3 and $ZnFe_2O_4$ photocatalysts. The relatively good photocatalytic performances observed for the Fe_2O_3-ZnO-S12 sample may be linked to its well-shaped rod-like structure and hierarchical microstructure. Indeed, the rod-like 1D structure is favorable for the separation of electron/hole pairs while the hierarchical microstructure improves the light harvesting and the increase of the specific surface area [51, 52]. The worst photodegradation efficiency observed for the Fe_2O_3-ZnO-S6 film likely originates from the spraying method that discriminates the formation of an heterostructured catalyst and from the decreased hierarchical microstructure. The comparison of the photodegradation performances of Fe_2O_3-ZnO films were also conducted based on the pseudo-first-order kinetics and results obtained show that Fe_2O_3-ZnO-M (0.0185 min^{-1}) > Fe_2O_3-ZnO-S12 (0.0044 min^{-1}) > Fe_2O_3-ZnO-S3 (0.0029 min^{-1}) > Fe_2O_3-ZnO-S6 (0.0007 min^{-1}) (Fig. 7d).

3.5 Influence of the films architecture on the photodegradation efficiency under visible light

The visible-light driven photocatalytic activities of these films were also evaluated for the degradation of Orange II. The time-evolutions of the UV-visible absorption spectra of the dye

when using CeO_2-ZnO and Fe_2O_3-ZnO films are shown in Fig. ~~S4~~ S5a–d and Fig. ~~S4~~ S5e-h, respectively. A relatively faster decrease of the characteristic peak of Orange II at 485 nm was observed ~~in~~ for the CeO_2-ZnO-M and CeO_2-ZnO-S3 samples. The corresponding plots of C_t/C_0 versus time for the CeO_2-ZnO samples are displayed in Fig. 8a. The CeO_2-ZnO-M sample efficiently decomposes Orange II (photodegradation of 62% within 360 min), and is followed by CeO_2-ZnO-S3 (55%), CeO_2-ZnO-S6 (40%), and CeO_2-ZnO-S12 (28%). These performances are consistent with the bandgaps determined for these materials (Fig. 6a). As the visible-light driven photodegradation is more limited by the absorption of photons than UV-driven photocatalysis, the bandgaps likely play more important roles compared to surface morphologies. The best performance of the CeO_2-ZnO-M sample is ascribed to the lowest bandgap of this composite, likely originating from an optimal hybridization between CeO_2 and ZnO phases. A similar hypothesis can be made for the CeO_2-ZnO-S3 sample, compared to the CeO_2-ZnO-S6 and CeO_2-ZnO-S12 films. The kinetics of the photodegradations with these CeO_2-ZnO films under visible light were illustrated in Fig. 8b. The order of reaction rate constant is CeO_2-ZnO-M (0.0026 min^{-1}) > CeO_2-ZnO-S3 (0.0019 min^{-1}) > CeO_2-ZnO-S6 (0.0015 min^{-1}) > CeO_2-ZnO-S12 (0.0012 min^{-1}) and further confirm that under visible light irradiation, better photocatalytic performance was achieved with CeO_2-ZnO-M and CeO_2-ZnO-S3 samples. It could be inferred that the non-laminated architecture and intermediately-laminated architecture with fewer deposition layers within each cycle is beneficial ~~benefitting~~ for the visible-light driven photodegradation.

The UV-visible absorption spectra of Orange II during its photodegradation using Fe_2O_3-ZnO films under visible light irradiation are displayed in Fig. ~~S4~~ S5e-h. The photodegradation performances of the films are also quite sensitive to the laminated architectures. For instance, using the non-laminated Fe_2O_3-ZnO-M sample, the ~~characteristic~~ peak at 485 nm nearly decreased to 0 after 360 min visible light irradiation (Fig. ~~S4~~ S5e), while weak changes of the dye UV-visible absorption intensity was achieved with the laminated Fe_2O_3-ZnO-S6 sample (Fig. ~~S4~~

S5g). The corresponding plots of C_t/C_0 for the various Fe_2O_3-ZnO samples under visible light irradiation are shown in Fig. 8c and confirm that up to 95% degradation was achieved using the Fe_2O_3-ZnO-M film after 360 min, followed by Fe_2O_3-ZnO-S12 (28.4%), Fe_2O_3-ZnO-S3 (22%) and Fe_2O_3-ZnO-S6 (15%). This order is the same than that obtained under UV light irradiation (Fig. 7c). When comparing these results with those obtained with CeO_2-ZnO samples, the lower bandgap is responsible for ~~of~~ the higher visible light-driven photodegradation efficiency obtained for the Fe_2O_3-ZnO-M film. The photodegradation kinetics of Fe_2O_3-ZnO samples are shown in Fig. 8d. The order of reaction rate constant is Fe_2O_3-ZnO-M (0.0093 min^{-1}) > Fe_2O_3-ZnO-S12 (0.001 min^{-1}) > Fe_2O_3-ZnO-S3 (0.0005 min^{-1}) > Fe_2O_3-ZnO-S6 (0.0003 min^{-1}), which is agreement with the photodegradation results (Fig. 8c).

3.6 ~~Potential reason for preferred laminated~~ Laminated architectures depend on the content of ~~for different~~ hetero-material catalysts ~~systems~~

The above results show that laminated architectures play a critical role on the surface morphologies, while the phase compositions and composition ratios were less affected ~~effected by the architectures~~. Thus, the different photodegradation performances under UV and visible light irradiation are connected to the surface morphologies. Fig. 3 and Fig. 4 demonstrate that the surface morphologies changed from conventional island-like microstructures for the non-laminated film to hierarchical morphologies composed of partly rod-like ZnO particles and fine particles (CeO_2, or Fe_2O_3 with $ZnFe_2O_4$) for the laminated films.

For the CeO_2-ZnO photocatalysts, as the CeO_2 phase possesses good intrinsic photoactivity ~~photoactivities~~ with a low recombination rate of photogenerated electron/hole pairs, the non-laminated architectures (i.e. CeO_2-ZnO-M) and the laminated architectures (e.g. CeO_2-ZnO-S3, CeO_2-ZnO-S6 and CeO_2-ZnO-S12) exhibit relative low differences in the utilization of light (Fig. 9a). This may explain the close photodegradation efficiencies of these materials as shown in Fig.

7a. It should be noted that the rod-like 1D structure is favorable for separation of hole/electron pairs and that the hierarchical microstructure is believed to improve light harvesting and to increase the specific surface area [51, 52]. In this case, the intermediately-laminated CeO_2-ZnO architecture with fewer deposition layers within each cycle (e.g. CeO_2-ZnO-S3) benefits from synergic effects of narrower bandgap due to better association of the two phases and from the hierarchical microstructures and well-shaped nanostructures originating from the separated injection mode.

For the Fe_2O_3-ZnO films, due to the poor intrinsic photoactivity of Fe_2O_3 and $ZnFe_2O_4$ phases, laminated architectures (e.g. Fe_2O_3-ZnO-S3, Fe_2O_3-ZnO-S6) exhibit a modest photocatalytic activity due to the presence of the Fe_2O_3 and $ZnFe_2O_4$ phases at the surface of the films (Fig. 9b). By contrast, the non-laminated architecture (i.e. Fe_2O_3-ZnO-M) benefits from the good combination between Fe_2O_3 and ZnO phases which allows a better separation of photogenerated electron/hole pairs, and thus a better photodegradation performance. It should be noted that the fully-laminated architecture (i.e. Fe_2O_3-ZnO-S12) exhibit a good photocatalytic activity due its hierarchical microstructure and well-shaped nanostructures, which promotes the exposition of photocatalytically active crystal planes combined to a higher surface area and a better utilization of photon energy.

3.7 Identification of the active species involved in the photodegradation ~~using~~ in CeO_2-ZnO and Fe_2O_3-ZnO films

The active species involved in the photodegradations mediated by CeO_2-ZnO-M and Fe_2O_3-ZnO-M films under UV light irradiation were also detected by trapping experiments. *Tert*-butanol *t*-BuOH ($^{\bullet}OH$ radical scavenger), *p*-benzoquinone (BQ) ($O_2^{\bullet-}$ radical scavenger), ammonium oxalate (hole h^+ scavenger) and DMSO (electron e^- scavenger) were added into the Orange II solution before irradiation ~~of the dispersions~~ [53-55]. The time-evolutions of the UV-visible

absorption spectra of Orange II during these photocatalytic experiments using CeO_2-ZnO-M and Fe_2O_3-ZnO-M are displayed in Fig. S6 ~~S5~~a-d and Fig. S6 ~~S5~~e-h, respectively. For both films, the photodegradations are sensitive to the presence of these scavengers. For example, using the CeO_2-ZnO-M sample, the intensity of the ~~characteristic~~ UV-visible absorption peak of Orange II only weakly decreased in the presence of BQ and ammonium oxalate, indicating that no degradation occurs. The corresponding plots of C_t/C_0 versus time clearly demonstrate that $O_2^{\bullet-}$ and h^+ play a key role in the photodegradation using the CeO_2-ZnO-M (Fig. 10a). For the Fe_2O_3-ZnO-M film, the same active species are involved in the degradation of the dye (Fig. 5e-h and 10b) and in both cases, these species are different from those identified using the pure ZnO film [37]. This change may be ascribed to the heterostructure built between ZnO and CeO_2, ~~or~~ Fe_2O_3 or $ZnFe_2O_4$, which allows an efficient transfer of charge carriers [56, 57].

4. Conclusion

In summary, heterostructured CeO_2-ZnO and Fe_2O_3-ZnO films with various laminated architectures were successfully prepared via the SPPS ~~solution precursor plasma spray (SPPS)~~ process. Intermediately-laminated (CeO_2-ZnO-S3, CeO_2-ZnO-S6, Fe_2O_3-ZnO-S3, Fe_2O_3-ZnO-S6) and fully-laminated (CeO_2-ZnO-S12 and Fe_2O_3-ZnO-S12) samples were synthesized using separated injection modes and characterized. Non-laminated (CeO_2-ZnO-M, Fe_2O_3-ZnO-M) films were prepared using the mixed solution of precursors. Various surface morphologies were obtained for CeO_2-ZnO and Fe_2O_3-ZnO films as observed by SEM. The influences of films architectures on the photodegradation performances were investigated. The photodegradation tests revealed that the degradation efficiencies were sensitive to the ~~laminated~~ architectures of films. For the CeO_2-ZnO films, almost 100% degradation was achieved under UV light irradiation using the CeO_2-ZnO-S3, CeO_2-ZnO-S6 samples, due to their rod-like microstructures and to the good combination between CeO_2 and ZnO phases. Under visible light irradiation,

CeO_2-ZnO-S3 and CeO_2-ZnO-M samples exhibit higher performance due to their decreased bandgap. Both under UV and visible light irradiation, intermediately-laminated samples with fewer layers in each deposition cycles were demonstrated to show the highest photocatalytic activity. For the Fe_2O_3-ZnO heterostructure, UV light-driven 100% and 95% degradation of the Orange II dye was achieved within 240 and 360 min using the Fe_2O_3-ZnO-M sample. The mixed solution of precursors is beneficial from the better combination between Fe_2O_3 and ZnO phases. Trapping experiments revealed that superoxide anion ($O_2^{\bullet-}$) and holes (h^+) played a key role in photodegradations mediated by both CeO_2-ZnO and Fe_2O_3-ZnO films. This work not only provides insight into the influence of laminated architectures on the photodegradation performance, supplying guidance for the further design of photocatalytic films, but also demonstrates the capabilities of the SPPS technique to prepare heterostructured films with various laminated architectures for photocatalytic applications.

Acknowledgements

The authors, Zexin YU and Meimei LIU, gratefully appreciate to the support from the China Scholarship Council (Grant No. 201504490038 and Grant No. 201604490072).

References

[1] L. Jing, W. Zhou, G. Tian, H. Fu, Surface tuning for oxide-based nanomaterials as efficient photocatalysts, Chem. Soc. Rev. 42(24) (2013) 9509-9549.

[2] S. Malato, P. Fernández-Ibáñez, M.I. Maldonado, J. Blanco, W. Gernjak, Decontamination and disinfection of water by solar photocatalysis: Recent overview and trends, Catal. Today 147(1) (2009) 1-59.

[3] M.M. Khin, A.S. Nair, V.J. Babu, R. Murugan, S. Ramakrishna, A review on nanomaterials for environmental remediation, Energy Environ. Sci. 5(8) (2012) 8075.

[4] A. Kolodziejczak-Radzimska, T. Jesionowski, Zinc Oxide-From Synthesis to Application: A Review, Materials (Basel) 7(4) (2014) 2833-2881.

[5] J. Choina, A. Bagabas, C. Fischer, G.U. Flechsig, H. Kosslick, A. Alshammari, A. Schulz, The influence of the textural properties of ZnO nanoparticles on adsorption and photocatalytic remediation of water from pharmaceuticals, Catal. Today 241 (2015) 47-54.

[6] S. Baruah, J. Dutta, Effect of seeded substrates on hydrothermally grown ZnO nanorods, J. Sol-Gel Sci. Technol. 50(3) (2009) 456-464.

[7] J.B. In, H.J. Kwon, D. Lee, S.H. Ko, C.P. Grigoropoulos, In situ monitoring of laser-assisted hydrothermal growth of ZnO nanowires: thermally deactivating growth kinetics, Small 10(4) (2014) 741-9.

[8] J. Wang, Y. Xia, Y. Dong, R. Chen, L. Xiang, S. Komarneni, Defect-rich ZnO nanosheets of high surface area as an efficient visible-light photocatalyst, Applied Catalysis B: Environmental 192 (2016) 8-16.

[9] T. Sun, J. Qiu, C. Liang, Controllable fabrication and photocatalytic activity of ZnO nanobelt arrays, The Journal of Physical Chemistry C 112(3) (2008) 715-721.

[10] Y. Xia, J. Wang, R. Chen, D. Zhou, L. Xiang, A Review on the Fabrication of Hierarchical ZnO Nanostructures for Photocatalysis Application, Crystals 6(11) (2016) 148.

[11] A. Mclaren, T. Valdes-Solis, G. Li, S.C. Tsang, Shape and size effects of ZnO nanocrystals on photocatalytic activity, J. Am. Chem. Soc. 131(35) (2009) 12540-12541.

[12] A. Dodd, A. McKinley, T. Tsuzuki, M. Saunders, Tailoring the photocatalytic activity of nanoparticulate zinc oxide by transition metal oxide doping, Mater. Chem. Phys. 114(1) (2009) 382-386.

[13] E.S. Jang, J.H. Won, S.J. Hwang, J.H. Choy, Fine tuning of the face orientation of ZnO crystals to optimize their photocatalytic activity, Adv. Mater. 18(24) (2006) 3309-3312.

[14] R. Saravanan, S. Karthikeyan, V. Gupta, G. Sekaran, V. Narayanan, A. Stephen, Enhanced photocatalytic activity of ZnO/CuO nanocomposite for the degradation of textile dye on visible light illumination, Materials Science and Engineering: C 33(1) (2013) 91-98.

[15] J. Xie, Z. Zhou, Y. Lian, Y. Hao, P. Li, Y. Wei, Synthesis of α-Fe2O3/ZnO composites for photocatalytic degradation of pentachlorophenol under UV–vis light irradiation, Ceram. Int. 41(2) (2015) 2622-2625.

[16] K. Mageshwari, D. Nataraj, T. Pal, R. Sathyamoorthy, J. Park, Improved photocatalytic activity of ZnO coupled CuO nanocomposites synthesized by reflux condensation method, J. Alloys Compd. 625 (2015) 362-370.

[17] I.-T. Liu, M.-H. Hon, L.G. Teoh, The preparation, characterization and photocatalytic activity of radical-shaped CeO2/ZnO microstructures, Ceram. Int. 40(3) (2014) 4019-4024.

[18] C.M. Magdalane, K. Kaviyarasu, J.J. Vijaya, B. Siddhardha, B. Jeyaraj, J. Kennedy, M. Maaza, Evaluation on the heterostructured CeO2/Y2O3 binary metal oxide nanocomposites for UV/Vis light induced photocatalytic degradation of Rhodamine-B dye for textile engineering application, J. Alloys Compd. 727 (2017) 1324-1337.

[19] C. Li, R. Chen, X. Zhang, S. Shu, J. Xiong, Y. Zheng, W. Dong, Electrospinning of CeO2–ZnO composite nanofibers and their photocatalytic property, Mater. Lett. 65(9) (2011) 1327-1330.

[20] N.M. Shooshtari, M.M. Ghazi, An investigation of the photocatalytic activity of nano α-Fe2O3/ZnO on the photodegradation of cefixime trihydrate, Chem. Eng. J. 315 (2017) 527-536.

[21] Y. Liu, L. Yu, Y. Hu, C. Guo, F. Zhang, X.W.D. Lou, A magnetically separable photocatalyst based on nest-like γ-Fe 2 O 3/ZnO double-shelled hollow structures with enhanced photocatalytic activity, Nanoscale 4(1) (2012) 183-187.

[22] L. Cheng, L. Liu, R. Li, J. Zhang, Liquid phase deposition of α-Fe2O3/ZnO heterojunction film with enhanced visible-light photoelectrocatalytic activity for pollutant removal, J. Electrochem. Soc. 164(12) (2017) H726-H733.

[23] C. Li, X. Zhang, W. Dong, Y. Liu, High photocatalytic activity material based on high - porosity ZnO/CeO2 nanofibers, Mater. Lett. 80 (2012) 145-147.

[24] N.K. Dey, M.J. Kim, K.-D. Kim, H.O. Seo, D. Kim, Y.D. Kim, D.C. Lim, K.H. Lee, Adsorption and photocatalytic degradation of methylene blue over TiO_2 films on carbon fiber prepared by atomic layer deposition, J. Mol. Catal. A: Chem. 337(1-2) (2011) 33-38.

[25] H.-J. Wang, Y.-Y. Sun, C.-F. Wang, Y. Cao, Controlled synthesis, cytotoxicity and photocatalytic comparison of ZnO films photocatalysts supported on aluminum matrix, Chem. Eng. J. 198-199 (2012) 154-162.

[26] S. Dosta, M. Robotti, S. Garcia-Segura, E. Brillas, I.G. Cano, J.M. Guilemany, Influence of atmospheric plasma spraying on the solar photoelectro-catalytic properties of TiO_2 coatings, Applied Catalysis B: Environmental 189 (2016) 151-159.

[27] Y. Xu, M. Shen, Fabrication of anatase-type TiO_2 films by reactive pulsed laser deposition for photocatalyst application, J. Mater. Process. Technol. 202(1-3) (2008) 301-306.

[28] Z. Yu, H. Moussa, M. Liu, R. Schneider, M. Moliere, H. Liao, Solution precursor plasma spray process as an alternative rapid one-step route for the development of hierarchical ZnO films for improved photocatalytic degradation, Ceram. Int. 44(2) (2018) 2085-2092.

[29] M.J. Fabra, M.L. Flores-López, M.A. Cerqueira, D.J. de Rodriguez, J.M. Lagaron, A.A. Vicente, Layer-by-layer technique to developing functional nanolaminate films with antifungal activity, Food and bioprocess technology 9(3) (2016) 471-480.

[30] C. Aita, J. DeLoach, R. Sorbello, Optical absorption behavior of ZrO_2–TiO_2 nanolaminate films, J. Appl. Phys. 94(1) (2003) 654-663.

[31] G. Lee, R.S. Katiyar, B.-K. Lai, C. Phatak, O. Auciello, Dielectric behavior related to TiO_x phase change to TiO_2 in TiO_x/Al_2O_3 nanolaminate thin films, MRS Communications 4(2) (2014) 67-72.

[32] T. Zhou, S. Tan, Y. Guo, L. Ma, M. Gan, H. Wang, X. Sun, H. Wang, A laminated spherical composite assembled by alternating polyaniline and titania nanosheets with enhanced visible-light photocatalytic activity, J. Alloys Compd. 652 (2015) 358-363.

[33] W. Xie, L. Zhong, Z. Wang, F. Liang, X. Tang, C. Zou, G. Liu, Photocatalytic performance of $Bi_2VO_{5.5}/Bi_2O_3$ laminated composite films under simulated sunlight irradiation, Solid State Sciences 94 (2019) 1-7.

[34] A. Nakajima, S. Matsui, S. Yanagida, Y. Kameshima, K. Okada, Preparation and properties of titania-$Cs_{2.5}H_{0.5}PW_{12}O_{40}$ hybrid films, Surf. Coat. Technol. 203(9) (2009) 1133-1137.

[35] A.E. Morales, E.S. Mora, U. Pal, Use of diffuse reflectance spectroscopy for optical characterization of un-supported nanostructures, Revista mexicana de física 53(5) (2007) 18-22.

[36] S. Danwittayakul, M. Jaisai, J. Dutta, Efficient solar photocatalytic degradation of textile wastewater using ZnO/ZTO composites, Applied Catalysis B: Environmental 163 (2015) 1-8.

[37] Z. Yu, H. Moussa, M. Liu, B. Chouchene, R. Schneider, W. Wang, M. Moliere, H. Liao, Tunable morphologies of ZnO films via the solution precursor plasma spray process for improved photocatalytic degradation performance, Appl. Surf. Sci. 455 (2018) 970-979.

[38] I. Kosacki, T. Suzuki, H.U. Anderson, P. Colomban, Raman scattering and lattice defects in nanocrystalline CeO2 thin films, Solid State Ionics 149(1-2) (2002) 99-105.

[39] Z. Yu, H. Moussa, Y. Ma, M. Liu, B. Chouchene, R. Schneider, M. Moliere, H. Liao, Oxygen-defective ZnO films with various nanostructures prepared via a rapid one-step process and corresponding photocatalytic degradation applications, J. Colloid Interface Sci. 534 (2019) 637-648.

[40] A. Umar, S. Kim, E.-K. Suh, Y. Hahn, Ultraviolet-emitting javelin-like ZnO nanorods by thermal evaporation: growth mechanism, structural and optical properties, Chem. Phys. Lett. 440(1-3) (2007) 110-115.

[41] J. López-Sánchez, A. Serrano, A. Del Campo, M. Abuín, O. Rodríguez de la Fuente, N. Carmona, Sol–gel synthesis and micro-raman characterization of ε-Fe_2O_3 micro-and nanoparticles, Chem. Mater. 28(2) (2016) 511-518.

[42] Y. Li, Y. Li, Y. Yin, D. Xia, H. Ding, C. Ding, J. Wu, Y. Yan, Y. Liu, N. Chen, Facile synthesis of highly efficient ZnO/ZnFe2O4 photocatalyst using earth-abundant sphalerite and its visible light photocatalytic activity, Applied Catalysis B: Environmental 226 (2018) 324-336.

[43] Z. Yu, H. Moussa, B. Chouchene, M. Liu, R. Schneider, W. Wang, M. Moliere, H. Liao, One-step synthesis and deposition of ZnFe2O4 related composite films via SPPS route for photodegradation application, Nanotechnology 30(4) (2018) 045707.

[44] P. Li, M. Lei, W. Tang, Raman and photoluminescence properties of α-Al2O3 microcones with hierarchical and repetitive superstructure, Mater. Lett. 64(2) (2010) 161-163.

[45] V.K. Jayaraman, A. Hernández-Gordillo, M. Bizarro, Importance of precursor type in fabricating ZnO thin films for photocatalytic applications, Materials Science in Semiconductor Processing 75 (2018) 36-42.

[46] K. Jayanthi, S. Chawla, K. Sood, M. Chhibara, S. Singh, Dopant induced morphology changes in ZnO nanocrystals, Applied Surface Science 255(11) (2009) 5869-5875.

[47] Z. Yu, H. Moussa, M. Liu, R. Schneider, M. Moliere, H. Liao, Heterostructured metal oxides-ZnO nanorods films prepared by SPPS route for photodegradation applications, Surf. Coat. Technol. 375 (2019) 670-680.

[48] L. Sun, R. Shao, L. Tang, Z. Chen, Synthesis of ZnFe2O4/ZnO nanocomposites immobilized on graphene with enhanced photocatalytic activity under solar light irradiation, J. Alloys Compd. 564 (2013) 55-62.

[49] M. Niu, F. Huang, L. Cui, P. Huang, Y. Yu, Y. Wang, Hydrothermal synthesis, structural characteristics, and enhanced photocatalysis of SnO_2/α-Fe_2O_3 semiconductor nanoheterostructures, ACS nano 4(2) (2010) 681-688.

[50] M. Mishra, D.-M. Chun, α-Fe_2O_3 as a photocatalytic material: A review, Applied Catalysis A: General 498 (2015) 126-141.

[51] X. Zhang, J. Qin, Y. Xue, P. Yu, B. Zhang, L. Wang, R. Liu, Effect of aspect ratio and surface defects on the photocatalytic activity of ZnO nanorods, Sci. Rep. 4 (2014) 4596.

[52] M. Gao, L. Zhu, W.L. Ong, J. Wang, G.W. Ho, Structural design of TiO_2-based photocatalyst for H_2 production and degradation applications, Catalysis Science & Technology 5(10) (2015) 4703-4726.

[53] S. Adhikari, A. Banerjee, N.K. Eswar, D. Sarkar, G. Madras, Photocatalytic inactivation of E. Coli by ZnO–Ag nanoparticles under solar radiation, RSC Advances 5(63) (2015) 51067-51077.

[54] F. Liang, Y. Zhu, Enhancement of mineralization ability for phenol via synergetic effect of photoelectrocatalysis of g-C3N4 film, Applied Catalysis B: Environmental 180 (2016) 324-329.

[55] F.-t. Li, Y. Zhao, Q. Wang, X.-j. Wang, Y.-j. Hao, R.-h. Liu, D. Zhao, Enhanced visible-light photocatalytic activity of active Al2O3/g-C3N4 heterojunctions synthesized via surface hydroxyl modification, J. Hazard. Mater. 283 (2015) 371-381.

[56] E. Sherly, J.J. Vijaya, L.J. Kennedy, Effect of CeO2 coupling on the structural, optical and photocatalytic properties of ZnO nanoparticle, J. Mol. Struct. 1099 (2015) 114-125.

[57] Y. Yuan, G.-F. Huang, W.-Y. Hu, D.-N. Xiong, B.-X. Zhou, S. Chang, W.-Q. Huang, Construction of g-C3N4/CeO2/ZnO ternary photocatalysts with enhanced photocatalytic performance, J. Phys. Chem. Solids 106 (2017) 1-9.

Figure captions:

Fig. 1. Schematic illustration of the films, including (a) CeO_2-ZnO-M and Fe_2O_3-ZnO-M, (b) CeO_2-ZnO-S3 and Fe_2O_3-ZnO-S3, (c) CeO_2-ZnO-S6 and Fe_2O_3-ZnO-S6 and (d) CeO_2-ZnO-S12 and Fe_2O_3-ZnO-S12.

Fig. 2. Deposition method used for the preparation of heterostructured CeO_2-ZnO and Fe_2O_3-ZnO films with various laminated architectures via the SPPS process.

Fig. 3. (a,c) XRD patterns and (b,d) Raman spectra of CeO_2-ZnO and Fe_2O_3-ZnO films.

Fig. 4. Surface morphologies of (a, b) CeO_2-ZnO-M, (c, d) CeO_2-ZnO-S3, (e, f) CeO_2-ZnO-S6 and (g, h) CeO_2-ZnO-S12 samples under low and high magnifications.

Fig. 5. Surface morphologies of (a, b) Fe_2O_3-ZnO-M, (c, d) Fe_2O_3-ZnO-S3, (e, f) Fe_2O_3-ZnO-S6 and (g, h) Fe_2O_3-ZnO-S12 samples under low and high magnifications.

Fig. 6. Plots of $(F(R \times h\nu)^2$ vs $h\nu$ of (a) CeO_2-ZnO films and (b) Fe_2O_3-ZnO films..

Fig. 7. (a, c) Photodegradation performances and (b, d) pseudo-first-order kinetics of the Orange II degradation under UV light irradiation for CeO_2-ZnO and Fe_2O_3-ZnO films.

Fig. 8. (a, c) Photodegradation performances and (b, d) pseudo-first-order kinetics of Orange II degradation under visible light for CeO_2-ZnO and Fe_2O_3-ZnO films.

Fig. 9. Schematic illustration for the excitation behavior of (a) CeO_2-ZnO and (b) Fe_2O_3-ZnO films under light irradiation.

Fig. 10. Influence of scavengers on the photodegradation performance of (a) CeO_2-ZnO-M and (b) Fe_2O_3-ZnO-M samples under UV light irradiation.

Table captions:

Table 1 Spraying parameters for different laminated CeO_2-ZnO and Fe_2O_3-ZnO films

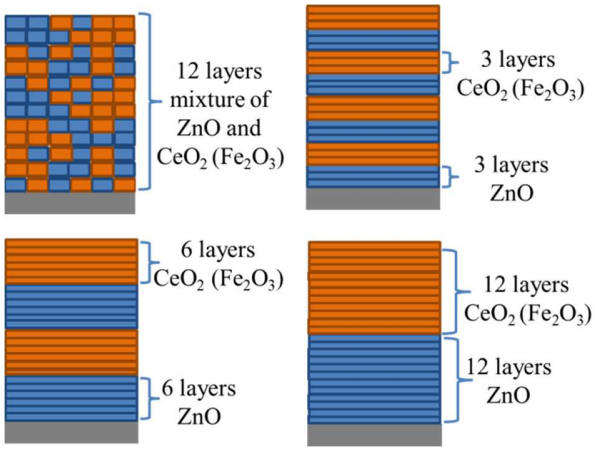

Fig. 1. Schematic illustration of the films, including (a) CeO_2-ZnO-M and Fe_2O_3-ZnO-M, (b) CeO_2-ZnO-S3 and Fe_2O_3-ZnO-S3, (c) CeO_2-ZnO-S6 and Fe_2O_3-ZnO-S6 and (d) CeO_2-ZnO-S12 and Fe_2O_3-ZnO-S12.

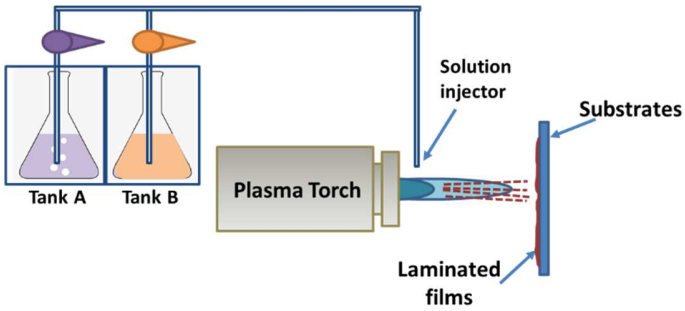

CeO_2 (Fe_2O_3)-ZnO-M: Tank A contains a mixture of zinc/cerium or zinc/iron precursors

CeO_2 (Fe_2O_3)- ZnO-S3/S6/S12: Tank A is the zinc solution and Tank B is the cerium or the iron solution

Fig. 2. Deposition method used for the preparation of heterostructured CeO_2-ZnO and Fe_2O_3-ZnO films with various laminated architectures via the SPPS process.

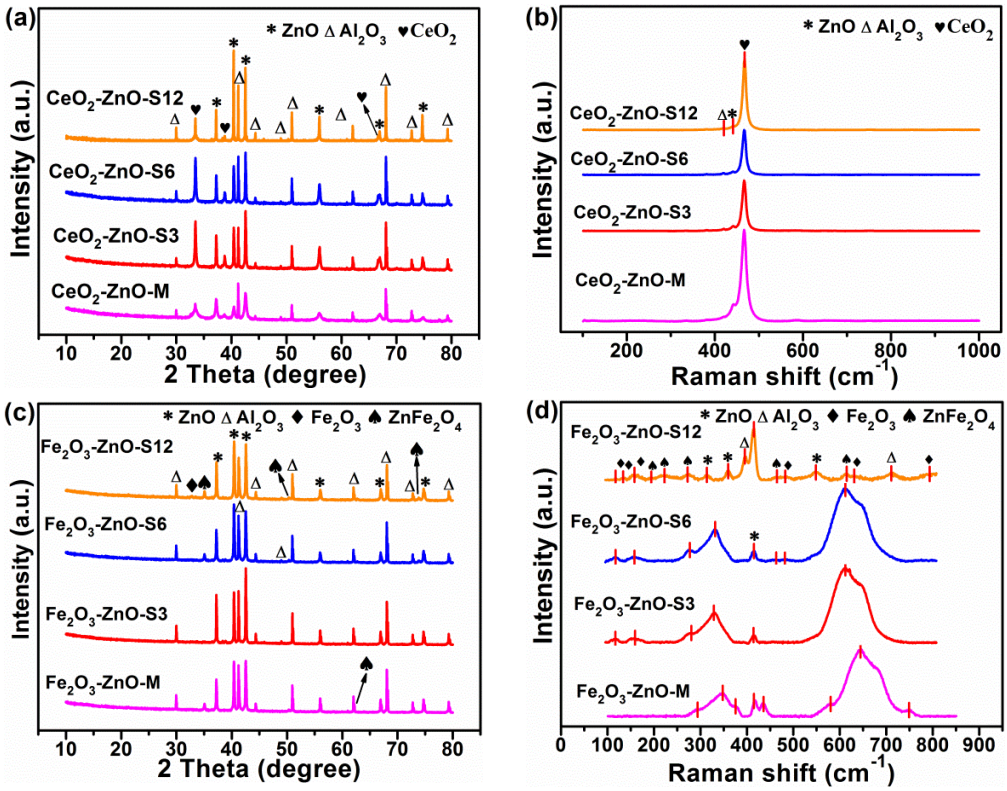

Fig. 3. (a,c) XRD patterns and (b,d) Raman spectra of CeO_2-ZnO and Fe_2O_3-ZnO films.

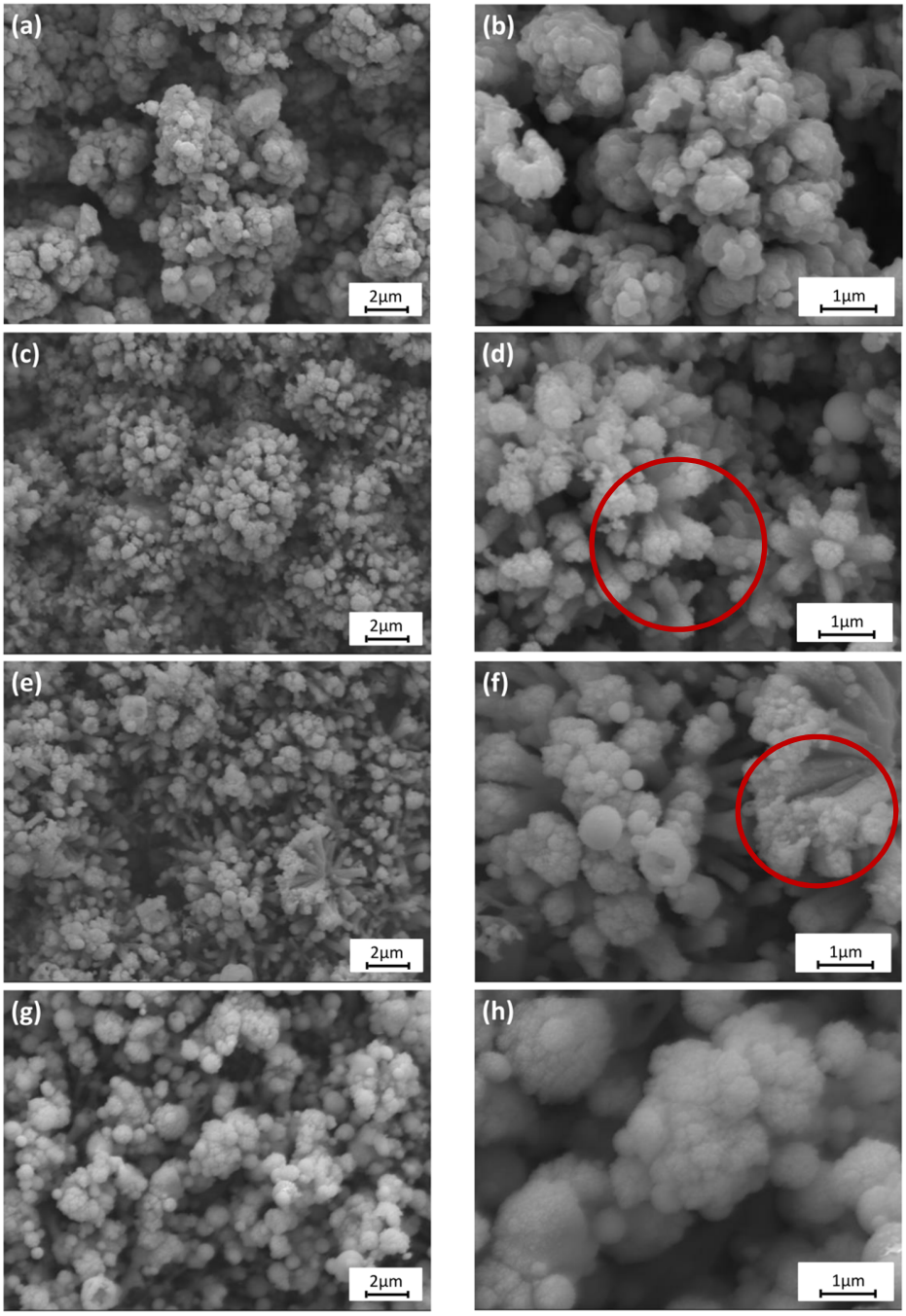

Fig. 4. Surface morphologies of (a, b) CeO_2-ZnO-M, (c, d) CeO_2-ZnO-S3, (e, f) CeO_2-ZnO-S6 and (g, h) CeO_2-ZnO-S12 samples under low and high magnifications.

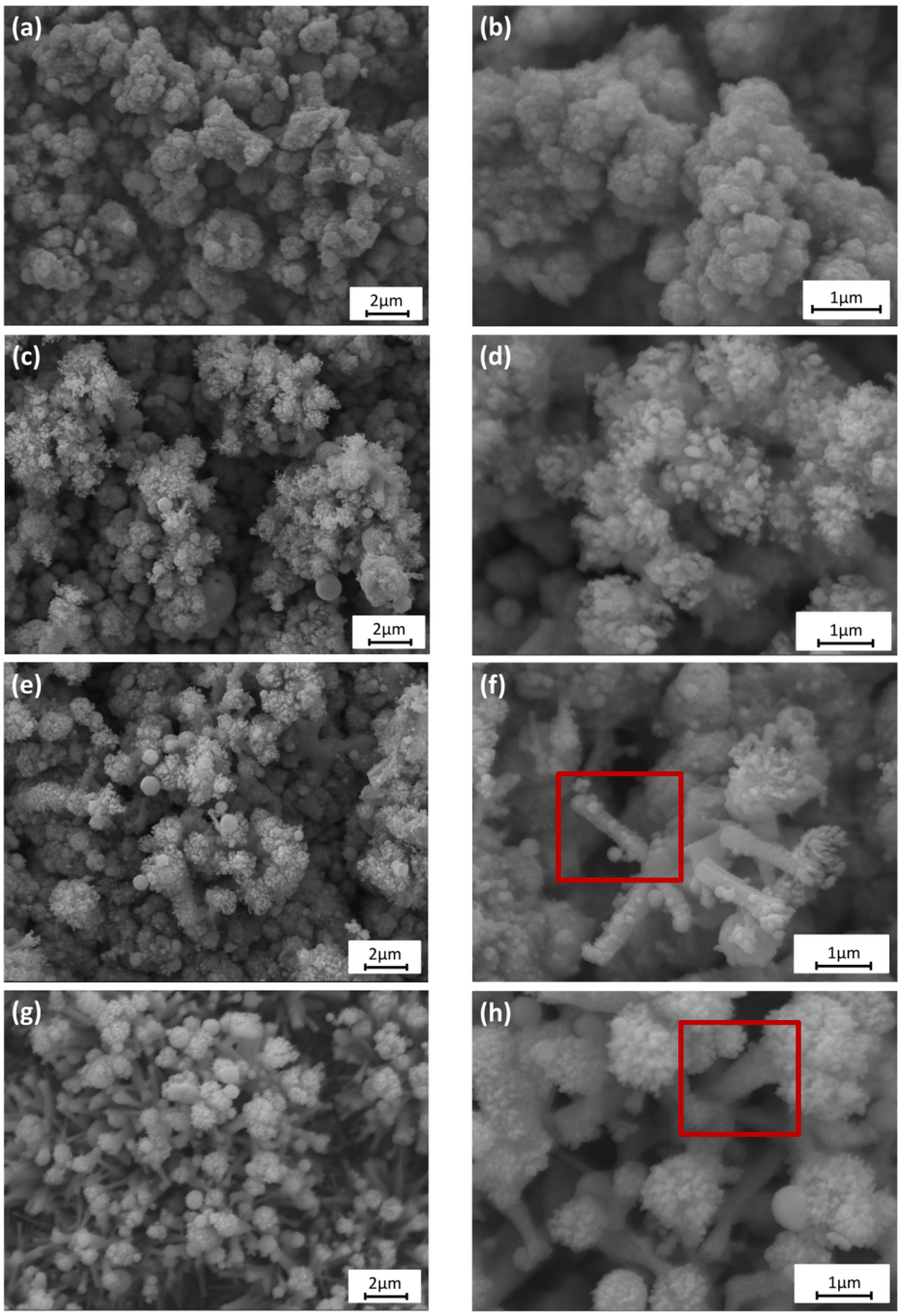

Fig. 5. Surface morphologies of (a, b) Fe_2O_3-ZnO-M, (c, d) Fe_2O_3-ZnO-S3, (e, f) Fe_2O_3-ZnO-S6 and (g, h) Fe_2O_3-ZnO-S12 samples under low and high magnifications.

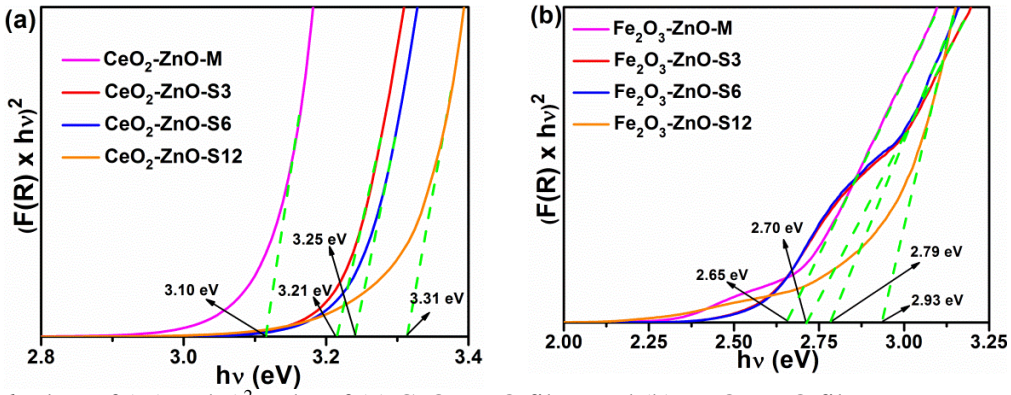

Fig. 6. Plots of $(F(R \times h\nu)^2$ vs hν of (a) CeO_2-ZnO films and (b) Fe_2O_3-ZnO films.

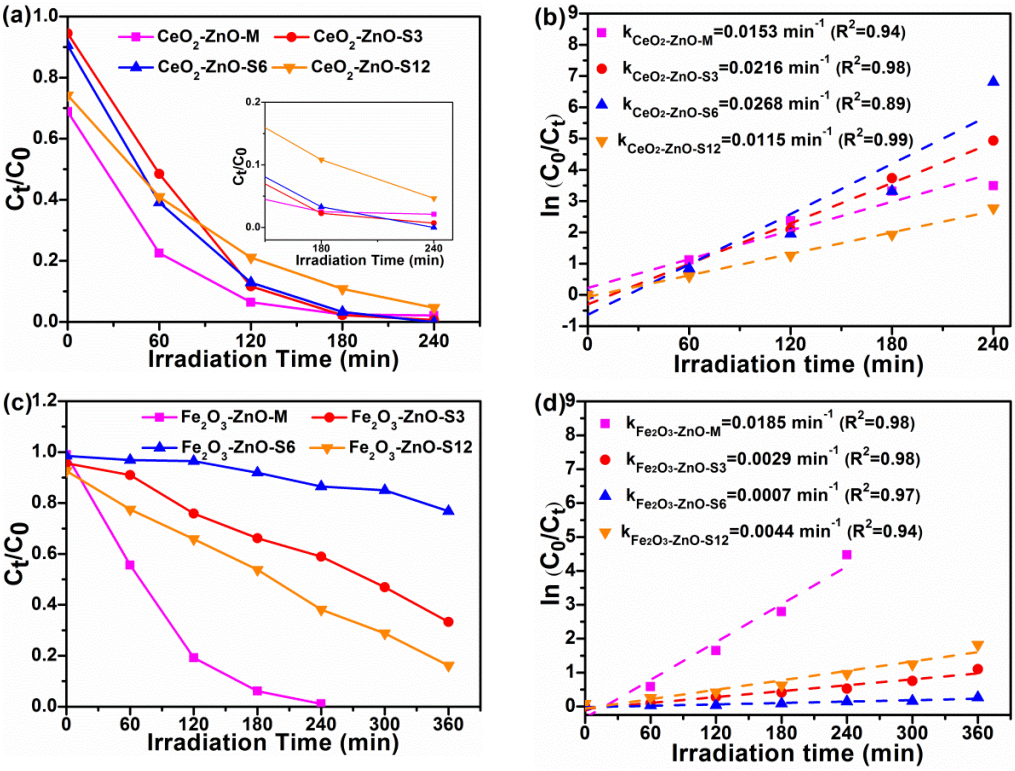

Fig. 7. (a, c) Photodegradation performances and (b, d) pseudo-first-order kinetics of the Orange II degradation under UV light irradiation for CeO_2-ZnO and Fe_2O_3-ZnO films.

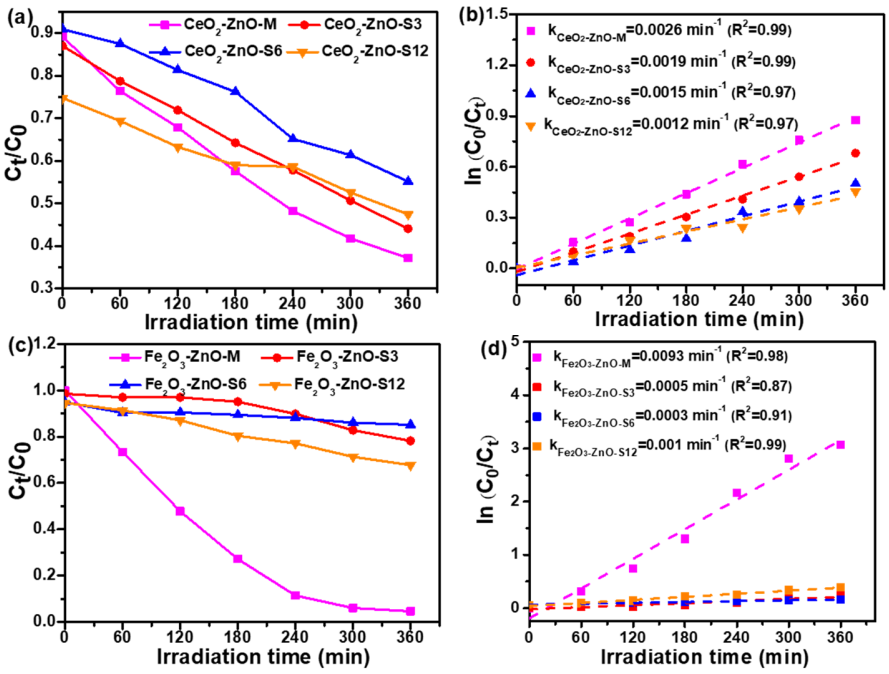

Fig. 8. (a, c) Photodegradation performances and (b, d) pseudo-first-order kinetics of Orange II degradation under visible light for CeO_2-ZnO and Fe_2O_3-ZnO films.

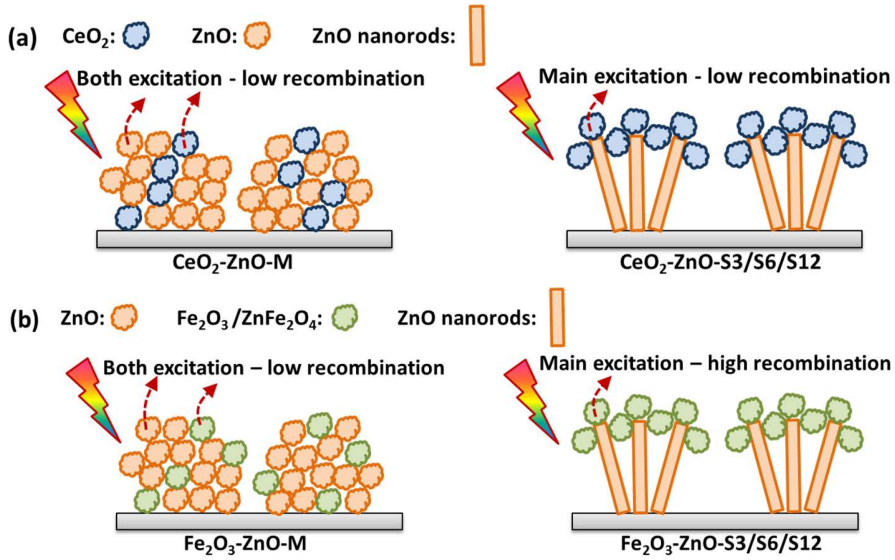

Fig. 9. Schematic illustration for the excitation behavior of (a) CeO_2-ZnO and (b) Fe_2O_3-ZnO films under light irradiation.

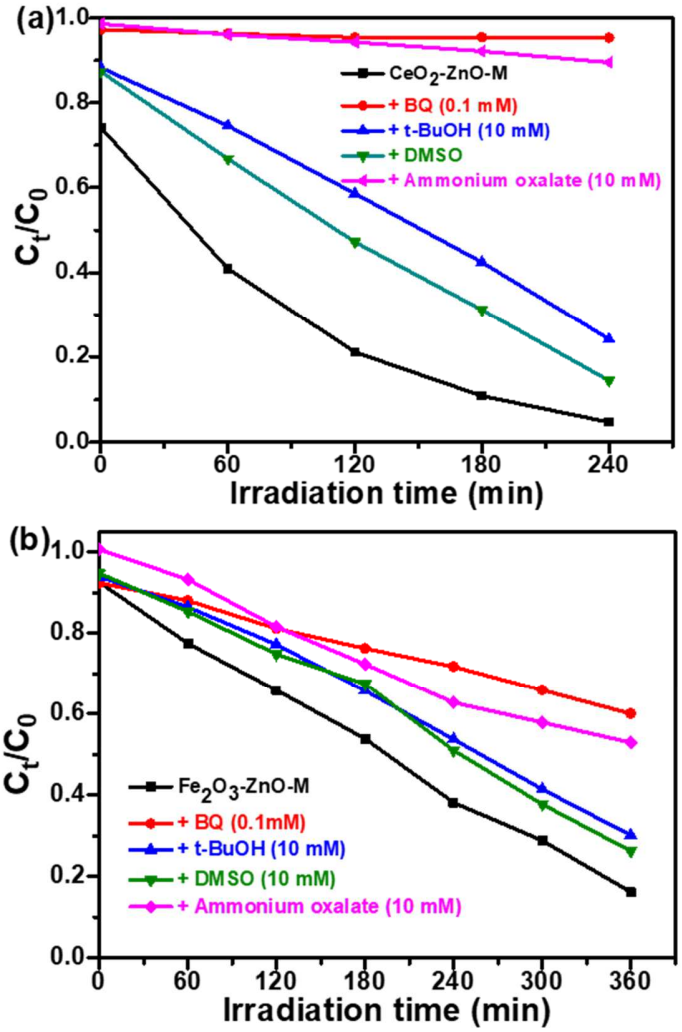

Fig. 10. Influence of scavengers on the photodegradation performance of (a) CeO_2-ZnO-M and (b) Fe_2O_3-ZnO-M samples under UV light irradiation.

Table 1. Spraying parameters for different laminated CeO_2-ZnO and Fe_2O_3-ZnO films

Parameters/ unit	CeO_2-ZnO-M Fe_2O_3-ZnO-M	CeO_2-ZnO-S3/S6/S12		Fe_2O_3-ZnO-S3/S6/S12	
		$Zn(OAc)_2$	$Ce(NO_3)_3$	$Zn(OAc)_2$	$Fe(NO_3)_3$
Torch power	30	30	30	30	30
Gas flow rate of Ar (L/min)	35	35	35	35	35
Gas flow rate of H_2 (L/min)	4	4	4	4	4
Current (A)	600	600	600	600	600
Spraying distance/ mm	90	90	90	90	90
Spraying cycles in each turn	12	3/6/12	3/6/12	3/6/12	3/6/12

Graphical abstract

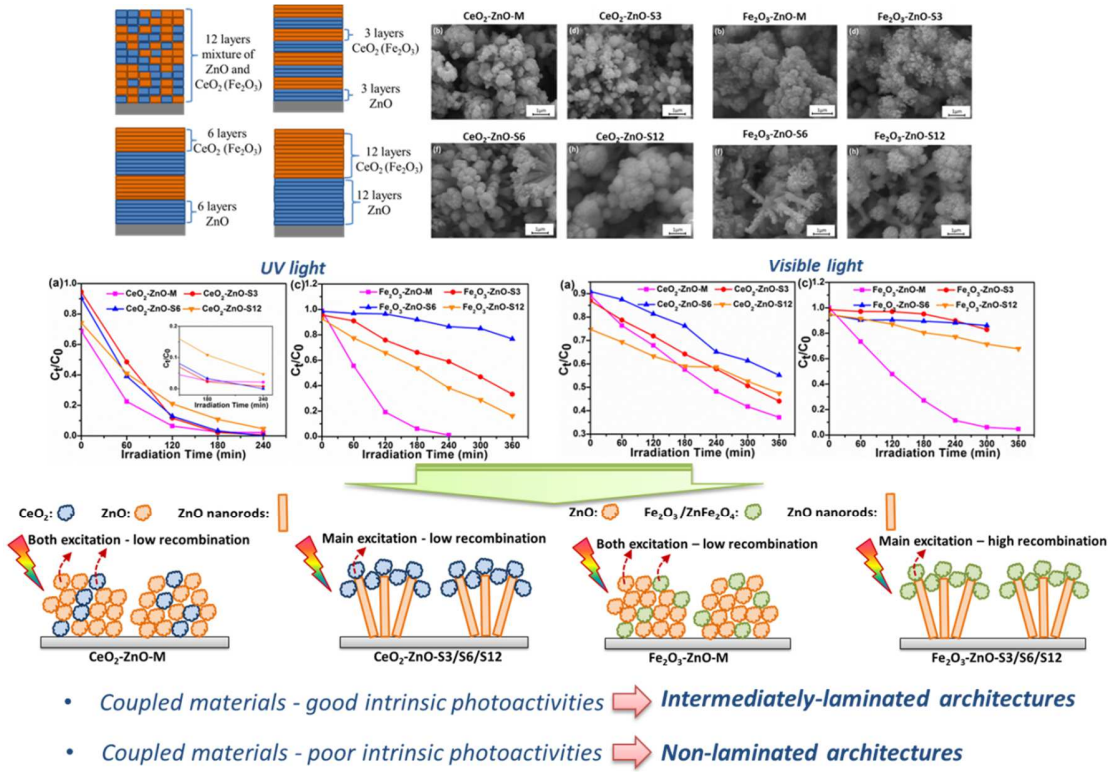

- *Coupled materials - good intrinsic photoactivities* ⇨ ***Intermediately-laminated architectures***
- *Coupled materials - poor intrinsic photoactivities* ⇨ ***Non-laminated architectures***